

Determination of the Age Distribution of Sea Ice from Lagrangian Observations of Ice Motion

Ronald Kwok, *Member, IEEE*, D. Andrew Rothrock, Harry L. Stern, and Glenn F. Cunningham

Abstract—A procedure for monitoring the local age distribution of the Arctic sea ice cover is presented. The age distribution specifies the area covered by ice in different age classes. In our approach, a regular array of grid points is defined initially on the first image of a long time series, and an ice tracker finds the positions of those points in all subsequent images of the series. These Lagrangian points mark the corners of a set of cells that move and deform with the ice cover. The area of each cell changes with each new image or time step. A positive change indicates that ice in a new age class was formed in the cell. A negative change is assumed to have ridged the youngest ice in the cell, reducing its area. The ice in each cell ages as it progresses through the time series. The area of multiyear ice in each cell is computed using an ice classification algorithm. Any area that is not accounted for by the young ice or multiyear ice is assigned to a category of older first-year ice. We thus have a fine age resolution in the young end of the age distribution, and coarse resolution for older ice. The age distribution of the young ice can be converted to a thickness distribution using a simple empirical relation between accumulated freezing-degree days and ice thickness, or using a more complicated thermodynamic model. We describe a general scheme for implementing this procedure for the Arctic Ocean from fall freeze-up until the onset of melt in the spring. The concept is illustrated with a time series of five ERS-1 SAR images spanning a period of 12 days. Such a scheme could be implemented with RADARSAT SAR imagery to provide basin-wide ice age and thickness information.

I. INTRODUCTION

THE age distribution of sea ice specifies the fractional area covered by ice in different age classes as a function of time. This ice distribution is a fundamental quantity that can be measured by ice tracking by keeping track of the area changes of deforming cells. In the Arctic Ocean in winter, new ice forms from freezing sea water that is exposed by the opening of leads in the ice cover. These horizontal openings manifest themselves as additions of areas to the local ice cover and are directly observable in time sequences of Synthetic Aperture Radar (SAR) imagery. The new ice in these leads ages and thickens. Repeated temporal sampling of these elemental areas provides us with an indication of when new areas or leads were created, the length of their existence, and thus a record of

Manuscript received Sept. 8, 1994.

This work was supported in part by the Applied Physics Laboratory, University of Washington under NASA contract, NAGW-2513 and in part by the Jet Propulsion Laboratory, California Institute of Technology under contract with the National Aeronautics and Space Administration.

R. Kwok and G. F. Cunningham are with the Jet Propulsion Laboratory, California Institute of Technology, Pasadena, CA 91109 USA.

D. A. Rothrock and H. L. Stern are with the Polar Science Center, Applied Physics Laboratory, College of Ocean and Fisheries Sciences, University of Washington, Seattle, WA 98195 USA.

IEEE Log Number 9408657.

their age. The resolution of age is dependent on the sampling interval. With some knowledge of the heat exchange between the atmosphere and ocean, the observed ice age distribution can be used to estimate the ice thickness distribution.

The estimation of the thickness distribution is the motivation for tracking the ice age distribution. Among the many properties of sea ice strongly dependent upon its thickness are compressive strength, rate of growth, surface temperature, turbulent and radiative heat exchange with the atmosphere, salt content and brine flux into the oceanic mixed layer [1]. Our present knowledge of the Arctic ice thickness distribution is derived largely from analysis of sonar data from submarine cruises. More recently, moorings with upward looking sonars have also been used to sample the thickness distribution at fixed locations. These and other remote sensing techniques under development for measurement of the ice thickness are reviewed in [2], [3]. These instruments typically provide a one dimensional transect of ice draft (or equivalently, thickness). The data are useful for computing the volume transport of ice through a region or building up a climatology of mean ice thickness over a long period of time.

In this paper, we describe a procedure that provides continual estimates of local age and thickness distributions of the Arctic sea ice cover. We note at the outset that the algorithm works only during the winter and also that it provides a fine age resolution of only the young end of the age distribution.

The method incorporates two algorithms that are operational in the Geophysical Processor System (GPS) at the Alaska SAR Facility (ASF). The current GPS routinely produces ice motion products and ice type images using ERS-1 SAR images as input [4]. Briefly, the ice tracking algorithm operates on pairs of images separated in time by three or more days, using a combination of area-matching and feature-matching techniques to track a regular array of points from the first image to the second image. This provides a set of ice displacement vectors on a fixed grid [5], [6]. The ice type algorithm uses a maximum likelihood classifier and a look-up table of expected backscatter characteristics to assign each image pixel to one of four classes: multiyear ice, deformed first-year ice, undeformed first-year ice, and a low backscatter type characteristic of smooth, younger ice types and calm open water [7]. These two algorithms are combined as follows.

II. OVERVIEW OF PROCEDURE

We assume that as a data source we have access to a long time sequence of SAR images acquired over some region of the Arctic Ocean. Initially, a regular array of points is defined

on the first image of the series. These points constitute the corners of a regular array of square cells, say, five kilometers on a side. The ice features at these points are identified and tracked in each of the subsequent images in the time series using the GPS ice tracking algorithm. Each point acquires its own trajectory, and the array of cells moves and deforms with the ice cover. This differs slightly from the current GPS ice tracking strategy, in which the motion from each pair of images is referred to an Earth-fixed grid, giving an Eulerian picture of the displacement field. Here, we use the tracking algorithm to follow the same set of points over a long time, giving a Lagrangian picture of the motion. We refer to the time interval between sequential images as a time step. During each time step the cell areas change. A positive change indicates that new ice was formed in the cell. A negative change is assumed to have ridged the youngest ice in the cell, reducing its area. The age classes are determined by the lengths of the time steps. The area of ice in each age class in each cell is updated at each time step. In this way, we keep track of the age distribution of the young ice.

The area of multiyear ice in each cell is also computed at each time step using the GPS ice classification algorithm. The classification accuracy for multiyear ice is around 95% [8]. Two possible sources of error are from wind-roughened open water and from frost flowers growing on new ice. Both of these physical phenomena result in highly variable radar backscatter, causing the classifier to label these pixels sometimes incorrectly as multiyear ice. The time series of multiyear ice area for each cell is used to resolve these ambiguities, resulting in a more accurate classification. Since the area of multiyear (MY) ice should remain constant (because no MY ice is created in the winter), any anomaly shows up as a transient spike or hump that can be filtered out. The filtering procedure is discussed in more detail in Section IV. The ice classification algorithm is not used to identify areas of first-year ice because the accuracy of the classifier is lower for these ice types. Since the areas of young ice and multiyear ice in each cell are accounted for by the procedures described above, and the total area of each cell is known from its geometry, the residual area is simply labeled as first-year ice. For a series of five images with, say, three days between successive images, the age classes would be: 0–3 days, 3–6 days, 6–9 days, 9–12 days, first-year ice, and multiyear ice.

Fields of surface air temperature from the National Meteorological Center (NMC) are assimilated by our algorithm and interpolated to the cell locations. With these temperatures throughout the times series, the young end of the age distribution can be converted to a thickness distribution using a simple empirical relation between accumulated freezing-degree days and ice thickness [9], or using a more complicated thermodynamic model. We note our scheme cannot say anything about the thickness of first-year or multiyear ice. The present method provides a two-dimensional, potentially basin-wide picture of the thickness of young ice, but it does not give any information about the mean thickness of the ice cover as a whole, since young ice occupies only a small fraction of the total area. The main output product of our age analysis procedure is the thickness distribution of young ice at a fine spatial resolution

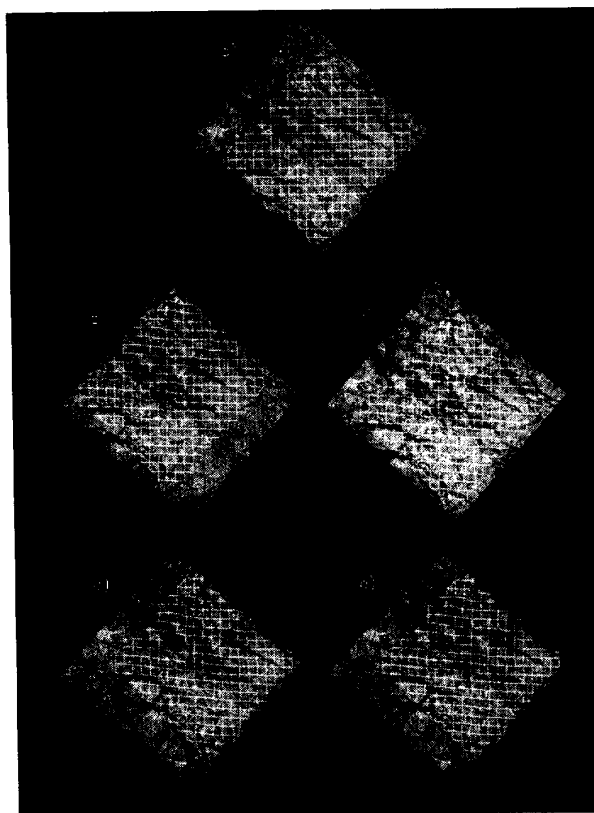


Fig. 1. Lagrangian observations of motion in SAR imagery. The five images (Image ID's: 15073, 15109, 15147, 15183, 16245) in the time sequence with overlaid deformation grids (the image product information is shown in Table I).

and the areal fraction of first-year and multiyear ice at regular time intervals.

When the Canadian Radarsat is launched in Jan. 1995, its imaging radar will have the capability to cover the entire Arctic Ocean every seven days with its wide swath (500 kilometer) ScanSAR mode [10]. We envision using this data and the procedure described herein to compute the age distribution of sea ice in the Arctic, starting at freeze-up in the fall and continuing until the onset of melt in the spring. The summer months cannot be treated because open water does not necessarily freeze into ice, and because the radar signature of multiyear ice in the summer is more variable.

Section III gives the computational and bookkeeping details of determining and updating the age distribution at each time step, including two examples from a time series of ERS-1 SAR images. Section IV outlines the general procedure for finding the age and thickness distributions throughout the winter, including some of the difficulties that still must be overcome. Concluding remarks are contained in the last section.

III. COMPUTATIONAL DETAILS AND EXAMPLES

First, we describe how we relate cell area changes to ice age. A *cell* is the area within an image defined by the straight-line segments connecting four grid or nodal points. Then,

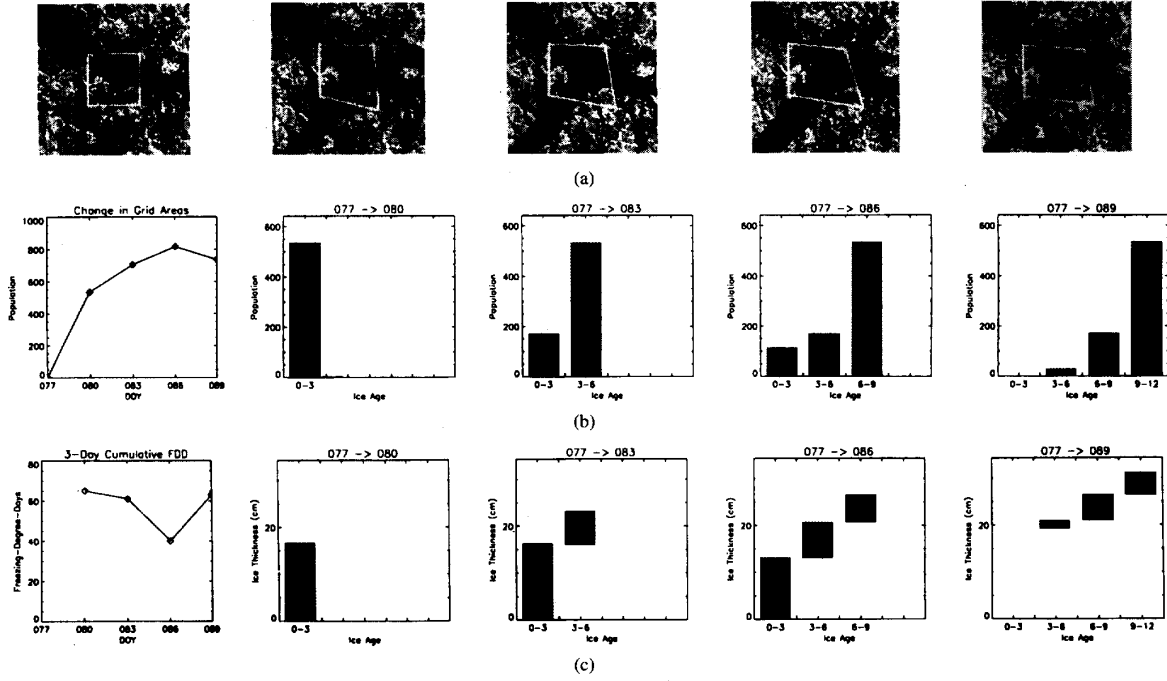


Fig. 2. Determination of ice age distribution and thickness distribution in a grid cell extracted from the time sequence (Example 1). (a) The image sequence showing the deformation of a grid cell. (b) Plot of area changes as a function of time, and age histograms computed from the area changes. (c) Plot of the freezing-degree days and the computed thickness of the ice. (1 pixel = 100m × 100m = 10000m² = unit area).

we discuss a computational procedure to determine the age distribution of ice within a cell. We want to estimate the areal contribution $B_{k,j}$ of each age category j at time t_k to the total observed area. The age resolution is dependent on the frequency of observation of a given cell. The sampling interval is constant in the examples shown here although this does not necessarily have to be the case. The general scheme for operating the procedure on a basin-wide scale is discussed in the next section.

A. Age from Cell Area Changes

Fig. 2 shows a cell in a sequence of five SAR images shown in Fig. 1. The increase in cell area, between Day 077 and Day 086, due to the continual opening of a lead, is evident. A closing event (between Day 086 and 089) caused a decrease in area of the cell. The area change during each time interval is plotted in Fig. 2(b). Any new area is assumed to have been produced between the time of the two images. Any loss in area is assumed to have depleted the area of the youngest ice created earlier. The multiyear ice area within the cell is estimated from the backscatter histogram from within the cell. These data are recorded and tabulated. Each record applies to the time of one scene and records the change since the last observation. These are the fundamental data for computing the age distribution. The age distribution, $B_{k,j}$, is a set of areas of different age classes. $B_{k,j}$ denotes the area of ice at time t_k of age category j . That is, the age of the ice satisfies the

TABLE I
IMAGE SEQUENCE (TIME, LOCATION, AND AVERAGE TEMPERATURE
Image Sequence (Time, Location and Average temperature)

Image No./ID	Time (DOY:HH)	Rev	Image Center	Temperature (°C)
1/15073	077:22	3509	73.29N/153.79W	-23
2/15109	080:22	3552	73.40N/153.64W	-20
3/15147	083:22	3595	73.29N/153.81W	-20
4/15183	086:22	3538	73.29N/153.82W	-19
5/16245	089:22	3581	73.30N/153.80W	-17

TABLE II
RECORD OF PARAMETERS (AREA CHANGES, AGE
DISTRIBUTION) FROM TIME-SEQUENCE ANALYSIS

Record	Time	Mean Temp, T	Cell Area, A	Age Distribution
				B
1	t_1		A_1	$B_{1,FY}, B_{1,MY}$
2	t_2	T_2	A_2	$B_{2,1}, B_{2,FY}, B_{2,MY}$
3	t_3	T_3	A_3	$B_{3,1}, B_{3,2}, B_{3,FY}, B_{3,MY}$
4	t_4	T_4	A_4	$B_{4,1}, B_{4,2}, B_{4,3}, B_{4,FY}, B_{4,MY}$
...
k	t_k	T_k	A_k	$B_{k,1}, B_{k,2}, \dots, B_{k,k-1}, B_{k,FY}, B_{k,MY}$

inequalities

$$t_k - t_{k-(j-1)} < age_{k,j} < t_k - t_{k-j} \quad \text{for } j = 2 \text{ to } k - 1.$$

We describe how the age table is constructed using the symbolic notation in Table II. Actual numerical examples are shown in a later section. The index k denotes time t_k ; the index j denotes age class, increasing with class age. T_k denotes the mean temperature during the time interval $[t_k, t_{k-1}]$; A_k is the area of the cell at time t_k .

The quantity $B_{k,MY}$ is the area of multiyear (MY) ice in the cell at time t_k , as determined from the backscatter

within the cell. We use the ice classification algorithm in the GPS for this purpose. Theoretically this should not depend on k (time), but errors in the classification of multiyear ice can result from wind-blown open water or frost flowers [8], [11]. These confounding effects can be identified and removed by considering the time series of the multiyear ice area: $B_{1,MY}, B_{2,MY}, \dots, B_{k,MY}$. This filtering problem is discussed later. The quantity $B_{k,FY}$ is the area of ice in the cell at time t_k older than $t_k - t_1$ but younger than multiyear ice, i.e., it is the older first-year (FY) ice. The oldest ice (other than FY and MY) which is observed in this procedure is dependent on the length of time required to “integrate” out the initial conditions (discussed in Section IV). At time t_1 , the area $B_{1,MY}$ is computed from the backscatter within the cell, as described above, and the area $B_{1,FY}$ is computed as the residual $A_1 - B_{1,MY}$.

B. Age Distribution Within a Cell

Suppose that the complete age histogram is known at time t_{k-1}

$$B_{k-1,1}, B_{k-1,2}, \dots, B_{k-1,k-2}, B_{k-1,FY}, B_{k-1,MY}$$

The computational procedure to obtain the histogram $B_{k,j}$ at time t_k is as follows:

- 1) The first step is a shift of the histogram that represents the aging process.

$$B_{k,j} \leftarrow B_{k-1,j-1} \quad \text{for } j = 2 \text{ to } k-1$$

For example, the first equation $B_{k,2} \leftarrow B_{k-1,1}$ says that the area of ice at time t_{k-1} (which was older than 0 but younger than $t_{k-1} - t_{k-2}$) is transferred into the class of ice that is older than $t_k - t_{k-1}$ but younger than $t_k - t_{k-2}$. In other words, we have added $\Delta t = t_k - t_{k-1}$ to the upper and lower bounds of the age class. A similar interpretation applies to the other equations. Note that $B_{k,1}$ is not defined yet. It is determined in the next step.

- 2) Compute the new total cell area, A_k , from the new positions of the grid points. Compute the change in cell area since the previous time: $\Delta A = A_k - A_{k-1}$. The area of the youngest ice class is now $B_{k,1} = \max(0, \Delta A)$. In other words, if new area was created ($\Delta A > 0$) then set the area of the youngest class to ΔA . If area was lost ($\Delta A < 0$) then set the area of the youngest class to zero. Step 4 accounts for any loss in area.
- 3) If $\Delta A \geq 0$ then skip to step 5.
- 4) This step is only executed when the cell area decreases ($\Delta A < 0$). We need to remove the area ΔA from the histogram. We first remove area from the next class $B_{k,2}$ and then older classes, as necessary, until a total area reduction of ΔA is achieved. The assumption is that we are ridging the youngest ice first.
- 5) The area of multiyear ice $B_{k,MY}$ is computed from the backscatter within the cell using the GPS ice classification algorithm.

- 6) The area of older first-year ice is computed as the residual area:

$$B_{k,FY} = A_k - [B_{k,1} + B_{k,2} + \dots + B_{k,k-1} + B_{k,MY}].$$

This completes the determination of the areas $B_{k,j}$ at time t_k . The procedure is repeated whenever Lagrangian observations of grid points are available.

C. Two Examples

1) Data Description

Time Series Dataset: We selected a time series of five ERS-1 SAR images to demonstrate the procedure for the determination of ice age distribution. Table I shows the temporal and spatial information related to the image frames within the time sequence. These images of the central Beaufort Sea were acquired in 1992 and span a period of 12 days from Mar. 18–30. The sampling interval or time step of the sequence is 3 days. The SAR images, each covering an area of approximately $100 \text{ km} \times 100 \text{ km}$ with pixel size of $100 \text{ m} \times 100 \text{ m}$, were processed at ASF and resampled to a polar stereographic projection.

Air Temperature: The 1000 mb air temperature field used in our analysis is a product distributed by the National Meteorological Center (NMC). These temperature fields are available twice daily at 0Z and 12Z. The temperature at the image center locations during the time of data acquisition are shown in Table I. We use the air temperature to compute the freezing-degree days which is used as input to the procedure for converting the ice age distribution into ice thickness distribution in Section IV.

Ice Tracking/Ice Typing: As previously mentioned, the present Geophysical Processor System has an ice tracker which produces an Eulerian ice motion product from image pairs. The tracker uses a combination of image matching by correlation of the image intensities and feature matching of the boundaries separating the ice types [5] to derive the displacement vectors at the grid points. The vectors give the displacements of the ice features initially defined on an Earth-fixed SSM/I grid ($\lambda_{SSM/I}, \phi_{SSM/I}$) to new geographic locations [$\lambda(\Delta t), \phi(\Delta t)$] in the interval Δt , separating an image pair. We modified the GPS ice tracker to generate the following time sequence of positions for each grid point over a sequence of k images to provide the trajectory of these grid points, viz.

$$\begin{aligned} [\lambda(t_1), \phi(t_1)] &\rightarrow [\lambda(t_2), \phi(t_2)] \rightarrow [\lambda(t_3), \phi(t_3)] \\ &\rightarrow \dots \rightarrow [\lambda(t_k), \phi(t_k)] \end{aligned}$$

where λ and ϕ represent the geographic location (longitude, latitude) of the points. The grid points and cells from the Lagrangian tracker are shown in Fig. 1. The dimension of the initial grid size is $5 \text{ km} \times 5 \text{ km}$.

The ice types used in our procedure are generated by the ice type classification algorithm in the GPS. The ice type algorithm utilizes first-order backscatter to classify pixel intensities into different ice types. The ice type product classifies Arctic winter SAR imagery into four ice types: multiyear (MY), first-year deformed (FY-D), first-year undeformed (FY-U) and a

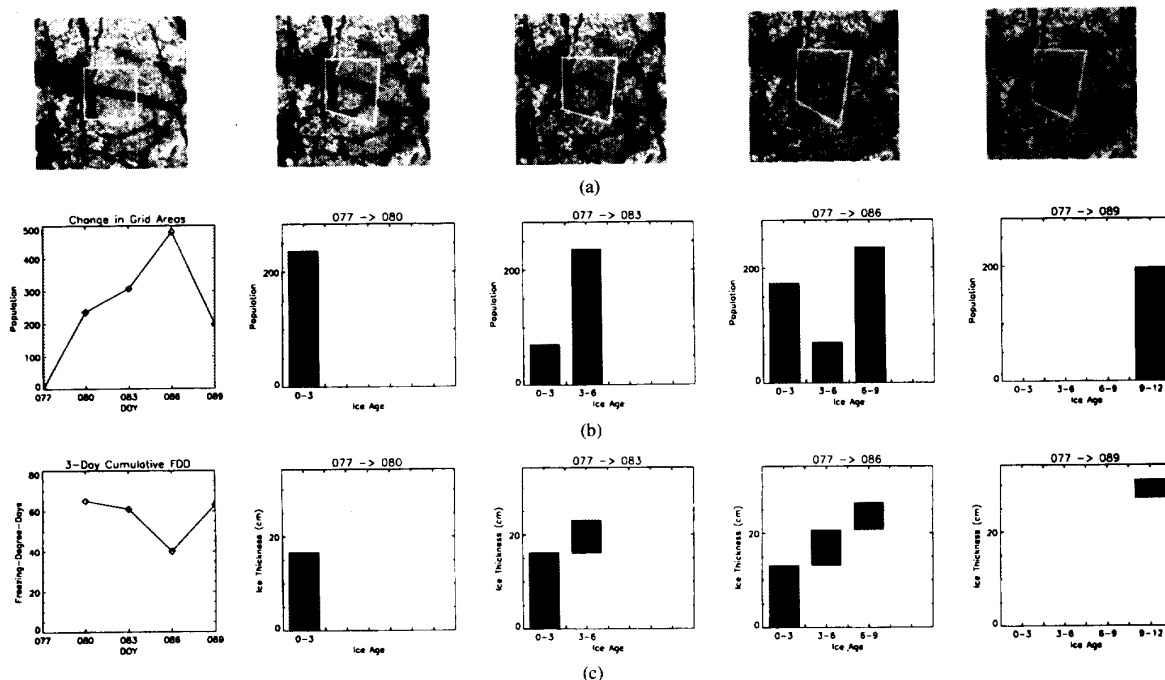


Fig. 3. Determination of ice age distribution and thickness distribution in a grid cell extracted from the time sequence (Example 2). (a) The image sequence showing the deformation of a grid cell. (b) Plot of area changes as a function of time, and age histograms computed from the area changes. (c) Plot of the freezing-degree days and the computed thickness of the ice. (1 pixel = $100\text{m} \times 100\text{m} = 10000\text{m}^2 = \text{unit area}$).

TABLE III
RECORD OF PARAMETERS (AREA CHANGES, AGE DISTRIBUTION)
FROM TIME-SEQUENCE ANALYSIS (EXAMPLE 1)

Record	Time (DAY:HH)	Mean Temp, T	Cell Area, A^*	FDD	Area* of Age Class j				FY	MY
					1	2	3	4		
1	077:22	-23	2500						1164	1336
2	080:22	-20	3034	65	534				598	1902
3	083:22	-20	3205	126	171	534			536	1964
4	086:22	-19	3317	166	112	171	534		1046	1454
5	089:22	-17	3235	229	0	30	171	534	1235	1265

* 1 pixel = $100\text{m} \times 100\text{m} = 10000\text{m}^2 = \text{unit area}$
FDD = Cumulative freezing-degree days

low backscatter type characteristic of smooth, younger ice types and calm open water. We emphasize, in this paper, that we use the ice classifier to determine only the MY fraction and that the interpretation of non-MY ice types does not present itself as an issue in our discussion.

2) Examples

Example 1: We are assuming, in the two examples here, that the initial distribution contains only FY and MY in the cells. Table III and Fig. 2 illustrate a few steps in the procedure. The increase in cell area, between Day 077 and Day 086, due to the continual opening of a lead, is evident. The area changes of the cell as a function of time are plotted in Fig. 2(b). This cell had an initial area of 2500 units, 1336 of which were classified as multiyear ice. Over the first time interval (Day 077 to Day 080), the area increased to 3034, giving a young ice class, $B_{2,1}$ (which is between 0–3 days old), an area of 534 units. The remaining 1164 units were assigned to the first-year ice class of undetermined age. The cell area increased to 3205

and 3317 during the second (Day 080 and 083) and third (Day 083 and 086) time intervals, respectively. This new area of 171 units created during the second time interval replaces the 534 units as the youngest age group. Similarly, the 112 units created during the third time interval replaces the 171 units as having the youngest age. The 534 units created during the first time interval have become 3–6 days and 6–9 days old, during the second and third time intervals, respectively, and represent the aging of the ice from $B_{2,2}$ to $B_{3,3}$. A closing event (between Day 086 and 089) caused a decrease in cell area from 3317 to 3235, or 82 units. At this time step, the newest age class ($B_{5,1} = 0$) has zero area since no new area was created, and the next youngest class loses 82 units to account for the lost cell area. 1265 units were classified as MY ice, leaving 1235 units of old FY ice. Note that the area of MY ice does not remain constant throughout the 12-day period. This is due to the high backscatter of the open lead, the signature of which overlaps with that of the MY ice backscatter, leading to an over estimation of MY ice. We discuss a procedure to resolve this classification error in the next section.

Example 2: Table IV shows the results from the temporal evolution of the grid cell in Fig. 3. The grid cell is extracted from the image time-series. This cell increased in area during the first three time intervals, with a decrease in area during the last time interval in the sequence. The total decrease in area of 284 units during the last time interval is accounted for by decreasing the area of the three youngest age classes. The MY ice area remained relatively constant during the whole time

TABLE IV
RECORD OF PARAMETERS (AREA CHANGES, AGE DISTRIBUTION)
FROM TIME-SEQUENCE ANALYSIS (EXAMPLE 2)

Record	Time (DAY:HH)	Mean Temp, T	Cell Area, A^*	FDD	Area* of Age Class j					
					1	2	3	4	FY	MY
1	077:22	-23	2500						692	1808
2	080:22	-20	2736	65	236				575	1925
3	083:22	-20	2807	126	71	236			612	1888
4	086:22	-19	2981	166	112	71	236		540	1960
5	089:22	-17	2697	229	0	0	0	197	588	1912

* 1 pixel = 100m × 100m = 10000 m² = unit area
FDD = Cumulative freezing-degree days

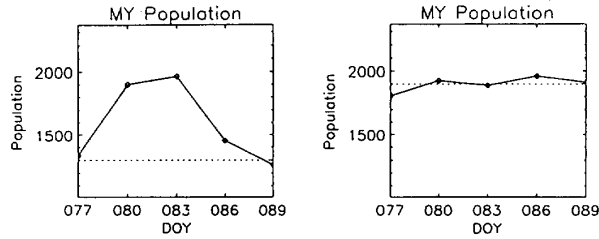


Fig. 4. Plot of the area of MY ice, $B_{k,MY}$, in the two grid cells. (a) Grid cell 1; (b) Grid cell 2. Dashed line shows the average MY area, A_{MY} , computed using the procedure in the text. (1 pixel = 100m × 100m = 10000m² = unit area).

sequence because the backscatter of the ice in the leads was low in this case.

IV. DISCUSSION OF GENERAL SCHEME

We have discussed the computation of the age distribution within a cell. Now, we address some of the unresolved technical issues associated with mechanizing such a scheme for observation of the age distribution of sea ice in the entire winter Arctic using a seasonal time sequence of SAR observations. The block diagram for the entire scheme is shown in Fig. 5.

A. Determination of Ice Age Distribution

Initial Conditions: The age distribution needs to be initialized at fall freeze-up. Since we do not know the ice age distribution at freeze-up, observations must be made for a period of time before the initial conditions or initial age distribution no longer affect the age distribution estimates. This start-up period is determined by the oldest age class (excluding FY and MY) we decide to track. For example, if the oldest desired age class is 30 days, then it will take 30 days for the initial conditions (young ice present at start-up) to grow into the FY category. Or, the initial distribution of ice in the 0–30 range would have “aged” beyond the range of observation. After this period, the initial conditions are determined and the age distribution will be correctly represented with the computational procedure above.

Multyear Ice Fraction: As previously noted, the presence of wind-blown open water or frost flowers on thinner ice could cause the ice classifier to over-estimate the area of multiyear ice even though the winter signature of multiyear ice has been shown to be stable [12]. Using the time series of multiyear ice for a particular cell, $B_{1,MY}, B_{2,MY}, B_{3,MY}, \dots$ these mis-

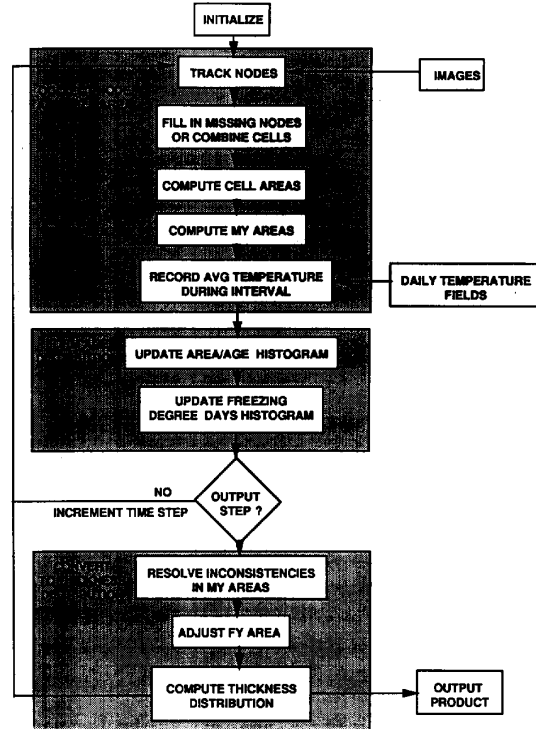


Fig. 5. Block diagram showing the general scheme.

classification events can be identified as positive spikes or humps. Filtering out these events leaves the “background” or true multiyear ice area. This may still not be perfectly constant since the cell boundaries (straight lines connecting the corner nodes) are not necessarily material boundaries and these moving edges can cause ice to shift into or out of a cell. Ideally,

$$A_k - A_{k-1} = \sum_{j=1}^N B_{k,j} - \sum_{j=1}^N B_{k-1,j} \quad j \neq MY$$

Or, all changes in cell area have to be accounted for by changes in area of the non-MY ice categories. The sum is over all non-MY categories. Here, we illustrate an alternate way to estimate an average area of MY ice, A_{MY} , using the time series of $B_{k,MY}$. Let $m = \min(B_{k,MY})$ for all k , and

$$S = \{k : B_{k,MY} < 1.1m\}.$$

Then,

$$A_{MY} = \text{Average}(B_{k,MY}) \quad \text{for } k \text{ in } S.$$

Or, the estimate of the MY ice fraction is given by the average of all $B_{k,MY}$ ’s less than 1.05 times the minimum of $B_{k,MY}$. The assumption is that mis-classification leads to an overestimate of MY ice and that the error in classification is approximately 5%. We use this simple procedure to estimate the average MY ice area. Fig. 5 shows $B_{k,MY}$ for the two grid cell examples used in the previous section; the dashed line indicates the average MY ice area, A_{MY} , determined

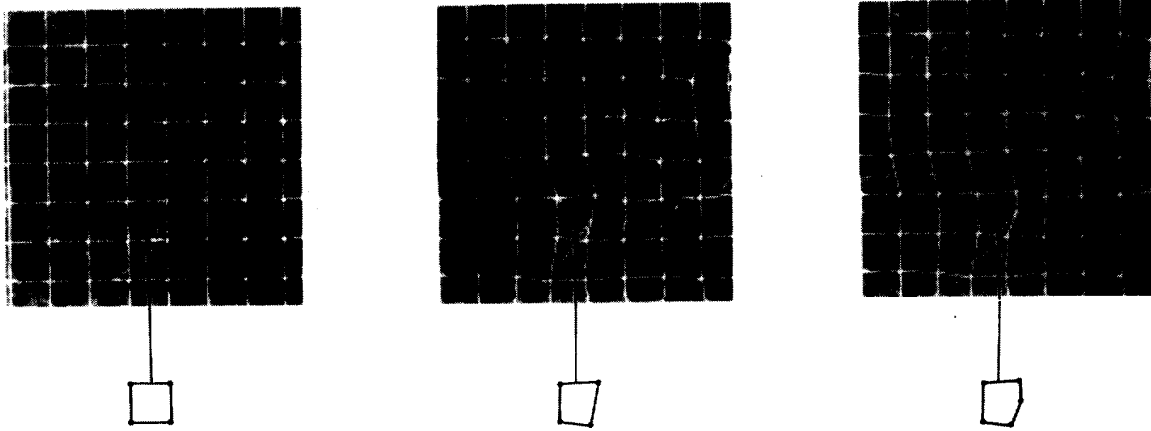


Fig. 6. Example showing the addition of a grid point when the strain between two grid points exceed a threshold of 1.1.

with this procedure. In the first example, the newly-opened lead has a backscatter signature which overlaps with that of MY ice and therefore increased the estimated areal fraction of MY ice in the grid cell. As the ice in the lead aged, its backscatter evolved toward a more FY ice-like signature and appearance, resulting in a decrease in area of MY ice. The MY ice area returned to approximately its area before the lead opened. The second example shows that the backscatter of the ice in the leads remained low and therefore did not confound the backscatter-based classifier. In both cases, a reasonable estimate of the MY ice fraction was obtained. Once the best estimate of multiyear ice at each time t_k is obtained from the filtered time series, the areas of older first-year ice $B_{k,FY}$ at each time t_k need to be adjusted as well, using the new value of $B_{k,MY}$.

Freezing-Degree Days: It is the freezing rate, not temperature or time alone, that tells the thermal history of each age class. To be able to convert age to ice thickness or to keep the required information when we interpolate ice age to a different grid, we must know the freezing rate. We approximate this rate as being proportional to the number of freezing-degree days (FDD) associated with each age class of each cell. In Table I, we have recorded the mean temperature, T_k , over each time interval $[t_k, t_{k-1}]$. We assume a suitable data product of surface air temperature from buoys and possibly NMC temperatures has been defined. It is obvious that the accuracy of the temperature field is important. The ice in the most recent age class $(k, 1)$ has a maximum FDD of

$$F_{k,1} = T_k(t_k - t_{k-1}).$$

All older classes have FDD equal to the sum of the $F_{*,1}$ back to their birth at time t_{k-j+1} :

$$F_{k,j} = F_{k,1} + F_{k-1,1} + F_{k-2,1} + \dots + F_{k-j+1,1} \quad \text{for } j = 2 \text{ to } k - 1$$

Hence, a record of the FDD is kept for each cell.

Missing Grid Points: Occasionally the tracking algorithm fails to find a match for a tie point. In the current GPS, this shows up simply as a hole in the displacement field.

For the long time sequence observations, where we want to keep track of cell properties, it means that for these cells the boundaries of four cells are not defined. We suggest the following alternatives to handle missing grid points:

- 1) Refine the matching/tracking scheme. Tracking fails because of low correlations between source and target images. This can happen if the tiepoint falls in a region undergoing a large deformation. Typically such regions are long and narrow. By placing the correlation window off-center with respect to the initial tie point location, it is possible that the new window will lie entirely on one rigid piece of ice, rather than spanning the zone between two moving pieces. This could help increase the correlation and identify more tiepoints that are very close to shear zones. Another option that is available to a Lagrangian tracker is to look at several previous images, rather than just the most recent image, when performing the correlation.
- 2) If a match still cannot be found, place the tie point in the most likely spot according to some interpolation scheme.
- 3) As an alternative to 2), combine the four cells around the missing nodal point into one big cell. This is an attractive procedure only if the frequency of resorting to this alternative is small, otherwise we will end up with large holes with no grid points.

Careful evaluation of these alternatives based on complexity and computational loading is required.

Regridding/Adding New Grid Points: As cells become "too deformed," nodes will have to be replaced by regridding. Adaptive regridding and moving meshes are techniques in use by finite element modelers. Two possible regridding strategies can be implemented: 1) Regrid each month (or other time interval) to a standard square grid; 2) Regrid locally when a cell becomes too deformed. Either of the options requires information such as area and freezing degree-days to be transferred or interpolated from an irregular grid to a regular one. We leave this as an issue here; suffice it to say that a strategy for addressing the deformation problem needs to be considered. An alternative to regridding is to create additional

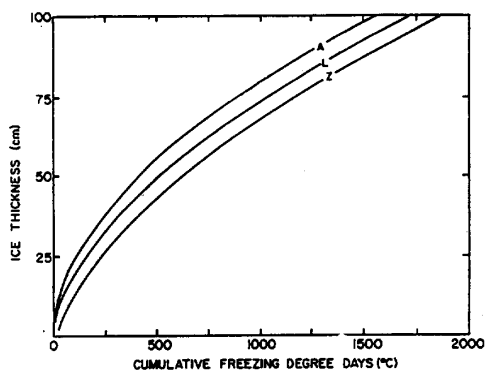


Fig. 7 Ice thickness as a function of freezing-degree days from the empirical formulas of Anderson (A), Lebedev (L), and Zubov (Z) [9].

grid points to define the cell boundaries if the deformation becomes too large. We illustrate this with an example (Fig. 6). In this case, the strain $(L - L_o)/L_o$ (L_o and L are the length of the line segments connecting two tiepoints before and after deformation, respectively) between two points exceeded a pre-set threshold (1.1) and a point was added between the two points. This minimizes the problem of uncertainty in the true material boundaries by maintaining a nominal sampling interval of the cell boundaries. We also note that when the deformation of an ice parcel is too high e.g., in the marginal ice zones, the gridding scheme suggested here may fail. In this case, we may have to avoid working close (less than 50 km) to the coast.

B. Conversion to Ice Thickness Distribution

We convert the age distribution, $B_{k,j}$, to the thickness distribution, $h_{k,j}$, with a simple procedure which utilizes the dependence of thickness, (H), on freezing-degree days, F ,

$$H_{k,j} = f(F_{k,j}).$$

For each area of young ice, $B_{k,j}$, there are upper and lower bounds on the age of the ice. Consequently there are two values of F , upper and lower bounds, that apply to each $B_{k,j}$. This corresponds to the maximum or upper bound on the freezing-degree days for the ice in that age class. The minimum or lower bound is $F_{k,j-1}$. We do not keep track of F for the FY and MY classes. Thus the thickness range of ice in $B_{k,j}$ is,

$$f(F_{k,j-1}) < h_{k,j} < f(F_{k,j}).$$

Fig. 7 plots three empirical relationships between the thickness of young sea ice and the cumulative number of freezing-degree days (after [9]). We used Lebedev's (1938) parameterization, with

$$H_{k,j} = 1.33F_{k,j}^{0.58}.$$

This relationship is based on 24 station-years of observations from various locations in the Soviet Arctic. Lebedev's parameterization describes ice growth under "average" snow conditions, in contrast to Anderson's which describes ice growth with little or no snow cover. The thickness of the snow cover is an important parameter which controls ice growth,

but there are no routine measurements available. Therefore, if we use an ice growth model with snow conditions as a parameter, we are dependent on a "climatological" description of the snow cover.

The upper and lower bounds of ice thickness for each age class are shown in Figs. 2(c) and 3(c). The high rate of ice growth when the ice is young gives the largest uncertainty in the thickness in this youngest age class. This uncertainty improves as the ice ages and the growth rate decreases. The area occupied by sea ice within a thickness range can be read directly from the Figs. 2(c) and 3(c). This completes the demonstration of our simple procedure for converting ice age into ice thickness. We have used a simple ice growth model to illustrate the process. Certainly, a more sophisticated thermodynamic model could be implemented to obtain the ice thickness, but the routine observations of some of the necessary atmospheric and oceanic parameters (e.g., snow depth, snow surface temperature, etc.) are not readily available.

V. CONCLUDING REMARKS

We have described the procedure for monitoring the local age distribution of sea ice for a large region. We have demonstrated the procedure using Lagrangian observations of ice motion obtained from a time sequence of ERS-1 SAR imagery. The advantage of this procedure is that it does not need to distinguish between the backscatter characteristics of thin and first-year ice types. The signature of multiyear ice has been shown to be strikingly stable over two winters [10]. The error in the estimation of the MY fraction, caused by frost flowers, wind-blown open water or pancake ice can be resolved with a time sequence of images. The MY ice fraction is an independent estimate and does not affect the age distribution of other age classes. Using an empirical relationship between ice growth and cumulative freezing-degree days or more sophisticated thermodynamic growth models, one can convert ice age to ice thickness.

In the general scheme, we suggest starting the process during fall freeze-up and continuing for the whole seasonal cycle through the onset of melt to obtain a record of the age distribution for the Arctic ocean. We have discussed some questions that need to be addressed before such a scheme could be mechanized for extended spatial and temporal observations. We have not addressed how such a scheme could be utilized for summer observations. The spatial and temporal coverage of the data required to sustain such a process are demanding. A sampling interval of six days would cause an uncertainty in ice age of six days and an uncertainty in the thickness of the thinnest ice of about 15 cm (if the air temperature were -30°C). The RADARSAT SAR, which will be launched in Jan. 1995, will have the capability to image the ice cover every six days. This scheme could be implemented in a new Geophysical Processor System to provide Arctic-wide fields of motion and age distributions.

REFERENCES

- [1] N. Untersteiner, Ed., *The Geophysics of Sea Ice*, Series B: Physics, vol. 146, New York: Plenum Press, 1986.

- [2] P. Wadhams and J. Corniso, "The ice thickness distribution inferred using remote sensing techniques," in F. D. Carsey, Ed., *Microwave Remote Sensing of Sea Ice*, Geophysical Monograph 68. Washington, DC: AGU, 1992.
- [3] A. S. Thorndike, C. Parkinson, and D. A. Rothrock, Eds., *Report of the Sea Ice Thickness Workshop*, Nov. 19–21, 1991, New Carrollton, MD: Appl. Physics Laboratory, Univ. Washington, 1992.
- [4] R. Kwok and T. Baltzer, "The geophysical processor system at the Alaska SAR Facility," *Photogramm. Eng. Remote Sensing*, to be published.
- [5] R. Kwok, J. C. Curlander, R. McConnell, and S. Pang, "An ice motion tracking system at the Alaska SAR facility," *IEEE J. Oceanic Eng.*, vol. 15, no. 1, pp. 44–54, 1990.
- [6] R. McConnell, R. Kwok, J. Curlander, S. Pang, and W. Kober, " ϕ -S correlation and dynamic time warping: Two methods for tracking ice floes in SAR images," *IEEE Trans. Geosci. Remote Sens.*, vol. 29, pp. 1004–1012, Nov. 1991.
- [7] R. Kwok, E. Rignot, B. Holt, and R. G. Onstott, "Identification of sea ice types in spaceborne SAR data," *J. Geophys. Res.*, vol. 97, no. C2, pp. 2391–2402, 1992.
- [8] F. Fetterer, D. Gineris, and R. Kwok, "Sea Ice type maps from Alaska SAR Facility imagery: An assessment" *J. Geophys. Res.*, vol. 99, no. C11, pp. 22443–22458, 1994.
- [9] G. A. Maykut, "The surface heat and mass balance," in N. Untersteiner, Ed., *Geophysics of Sea Ice*, Series B: Physics, vol. 146. New York: Plenum, 1986, p. 423.
- [10] R. K. Raney, A. P. Luscombe, E. J. Langham, and S. Ahmed, "RADARSAT," *Proc. IEEE*, vol. 79, June 1991.
- [11] K. Steffen, J. Heinrichs, J. Maslanik, and J. Key, "Sea ice feature and type identification in merged ERS-1 SAR and Landsat thematic mapper imagery," *Proc. 1st ERS-1 Symp.—Space Service Environ.*, Cannes, France, 1992, pp. 361–365.
- [12] R. Kwok and G. Cunningham, "Backscatter characteristics of the sea ice cover in the winter Beaufort Sea," *J. Geophys. Res.*, vol. 99, no. C4, pp. 7787–7802, 1994.



Ronald Kwok (M'86) received the B.Sc. degree from Texas A&M University, College Station, TX and the Ph.D. degree from Duke University, Durham, NC in 1976 and 1980, respectively.

He was a Postdoctoral Fellow at the University of British Columbia, Vancouver, BC, Canada in 1981. In 1985, he joined the Radar Science and Engineering Section at the Jet Propulsion Laboratory, Pasadena, CA, where he is currently the Group Supervisor of the SAR Systems Development and Processing Group responsible for research and

development of analysis and processing techniques for SAR data. His current interests include the application of remote sensing to the study of land and sea ice.

Dr. Kwok is a member of the American Geophysical Union, American Meteorological Society, Electromagnetics Academy, Tau Beta Pi, Phi Kappa Phi and Eta Kappa Nu.



D. Andrew Rothrock received the B.S. degree from Princeton University, Princeton, NJ, and the Ph.D. degree in fluid mechanics from the University of Cambridge, Cambridge, UK, in 1964 and 1968, respectively.

After teaching mathematics for a year at the Indian Institute of Science, Bangalore, India, he joined the University of Washington, Seattle, where he is presently an Associate Professor of Oceanography. He is the Principal Investigator of a NASA Earth Observing System interdisciplinary investigation directed at applying satellite data to these problems. His interests include polar heat exchange, sea ice mass balance, and the surface forcing and response of polar oceans.

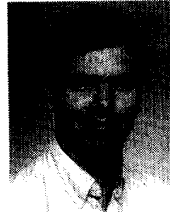
Dr. Rothrock is a member of the American Geophysical Union and the International Glaciological Society.



Harry L. Stern received the B.S. degree in mathematics from Stanford University, Stanford, CA and the M.S. degree in applied mathematics from the University of Washington, Seattle, in 1980 and 1982, respectively.

He joined the Polar Science Center at the University of Washington in 1987. He currently analyzes sea ice dynamics using information derived from synthetic aperture radar (SAR) images of the Arctic Ocean acquired by the ERS-1 satellite. He has developed algorithms and software for examining the structure and deformation of the arctic ice pack. He has also worked with SAR images from the Seasat satellite and from aircraft.

Mr. Stern is a member of the American Geophysical Union.



Glenn F. Cunningham received the B.A. degree in meteorology and the M.S. degree in atmospheric sciences at the University of California at Los Angeles in 1979 and 1982, respectively.

He has worked at the Jet Propulsion Laboratory in Pasadena, CA since 1979, where his work has involved studies of the SEASAT VIRR and Scatterometer data sets. Other work has included scatterometry model function analysis and algorithm development for the TOPEX project. He is currently a Member of the Technical Staff in the Radar

Science and Engineering Section conducting research with SAR data of the polar ice caps and developing science algorithms for RADARSAT SAR geophysical processing.